

Orbital *XY* models in moiré superlattices

Yanqi Li(李彦琪), Yi-Jie Wang(王一杰), and Zhi-Da Song(宋志达)

Citation: Chin. Phys. B, 2025, 34 (**2**): 027303. DOI: 10.1088/1674-1056/ad9ffc
Journal homepage: http://cpb.iphy.ac.cn; http://iopscience.iop.org/cpb

What follows is a list of articles you may be interested in

Manipulation of internal blockage in triangular triple quantum dot

Yue Qi(齐月) and Jian-Hua Wei(魏建华)
Chin. Phys. B, 2024, 33 (**5**): 057301. DOI: 10.1088/1674-1056/ad2d54

Real-time dynamics in strongly correlated quantum-dot systems

Yong-Xi Cheng(程永喜), Zhen-Hua Li(李振华), Jian-Hua Wei(魏建华), and Hong-Gang Luo(罗洪刚)
Chin. Phys. B, 2023, 32 (**12**): 127302. DOI: 10.1088/1674-1056/acf448

Chiral current regulation and detection of Berry phase in triangular triple quantum dots

Yue Qi(齐月), Yi-Ming Liu(刘一铭), Yuan-Dong Wang(王援东), Jian-Hua Wei(魏建华), and Zhen-Gang Zhu(朱振刚)
Chin. Phys. B, 2023, 32 (**8**): 087304. DOI: 10.1088/1674-1056/acd36c

Delayed response to the photovoltaic performance in a double quantum dots photocell with spatially correlated fluctuation

Sheng-Nan Zhu(祝胜男), Shun-Cai Zhao(赵顺才), Lu-Xin Xu(许路昕), and Lin-Jie Chen(陈林杰)
Chin. Phys. B, 2023, 32 (**5**): 057302. DOI: 10.1088/1674-1056/ac8e97

Thermoelectric signature of Majorana zero modes in a T-typed double-quantum-dot structure

Cong Wang(王聪) and Xiao-Qi Wang(王晓琦)
Chin. Phys. B, 2023, 32 (**3**): 037304. DOI: 10.1088/1674-1056/ac92d3

SPECIAL TOPIC — Moiré physics in two-dimensional materials

Orbital XY models in moiré superlattices

Yanqi Li(李彦琪)[1], Yi-Jie Wang(王一杰)[1,†], and Zhi-Da Song(宋志达)[1,2,3,‡]

[1] *International Center for Quantum Materials, School of Physics, Peking University, Beijing* 100871, *China*
[2] *Hefei National Laboratory, Hefei* 230088, *China*
[3] *Collaborative Innovation Center of Quantum Matter, Beijing* 100871, *China*

(Received 26 October 2024; revised manuscript received 11 December 2024; accepted manuscript online 17 December 2024)

Moiré superlattices provide a new platform to engineer various many-body problems. In this work, we consider arrays of quantum dots (QD) realized on semiconductor moiré superlattices with a deep moiré potential. We diagonalize single QD with multiple electrons, and find degenerate ground states serving as local degrees of freedom (qudits) in the superlattice. With a deep moiré potential, the hopping and exchange interaction between nearby QDs become irrelevant, and the direct Coulomb interaction of the density–density type dominates. Therefore, nearby QDs must arrange the spatial densities to optimize the Coulomb energy. When the local Hilbert space has a two-fold orbital degeneracy, we find that a square superlattice realizes an anisotropic XY model, while a triangular superlattice realizes a generalized XY model with geometric frustration.

Keywords: moiré superlattices, quantum dots, XY model

PACS: 73.21.La

DOI: 10.1088/1674-1056/ad9ffc **CSTR:** 32038.14.CPB.ad9ffc

1. Introduction

The lattice mismatch due to different lattice constants or a relative twist of two 2D material layers leads to the moiré superlattice.[1–3] Thanks to the highly adjustable energy band structure, e.g., by twist angle, strain, and external fields,[4,5] moiré superlattices have provided a new platform to engineer flat bands, where abundant correlated phases can be studied.[6–11] Recently, there is a focus on semiconductor moiré materials (SMS). In WX_2/MoX_2 ($X = S, Se$), the Hubbard model is studied[12] theoretically, and 2D triangular-lattice Hubbard model has been realized in aligned WSe_2/WS_2 experimentally.[13] Kane–Mele–Hubbard physics is identified in twisted $MoTe_2$.[14] Recently, the fractional quantum anomalous Hall states in twisted $MoTe_2$ have been experimentally found,[15–18] which drew great attention.

While the correlation in the topological flat bands has been a focus in SMS,[14,16,19] atomic flat bands can be intriguing as well. These SMS can realize arrays of quantum dots (QD), and new correlated phenomena can occur inside each QD, or arise from inter-QD couplings. In twisted bilayer WS_2, Li *et al.* have observed the formation of three-lobed "Wigner molecules" in each QD at $\nu = 3$ electrons per QD, which align into a Wigner molecule crystal on the superlattice.[20] The condition for the Wigner molecules to form is systematically studied by Ref. [21], and the ground states at more general fillings are investigated by Refs. [22,23]. The manipulation of internal blockage in triangular triple quantum dots has been studied by Qi *et al.*[24] The results demonstrated vast opportunities in designing and manipulating the QD ground states. Therefore, it will be natural to ask whether new correlated physics can be explored when multiple QDs are coupled in the superlattice.

In this article, we focus on SMS with a deep moiré potential, whose modulation amplitude V far exceeds the characteristic kinetic energy, $V \gg \frac{h^2}{2ma_M^2}$, where m is the effective mass, a_M is the moiré period, and $h = 2\pi\hbar$ is the Planck constant. In such a limit, QDs form at the periodic minima of the moiré potential, and the N-fold degenerate ground states in each QD effectively realize a "qudit" with an N-dimensional local Hilbert space. In general, N depends on the occupation number ν, and is protected by symmetry. Below the gap to the QD excited states $\hbar\omega_\star$, the lattice problem effectively reduces to a model of the qudits, with the model parameters determined by the inter-QD couplings.

In general, inter-QD couplings include kinetic hopping and Coulomb interactions, which can be either of the direct-type (density–density) or the exchange type. Let us denote the characteristic spatial spread of each qudit as ξ, beyond which the qudit wave-functions decay exponentially. For cosine-like moiré potentials, up to $O(1)$ factors, $\frac{\xi}{a_M} \propto (\frac{h^2}{2ma_M^2 V})^{1/4} \ll 1$ in the deep moiré potential limit. Since both the kinetic hopping and exchange-type Coulomb interactions are proportional to the inter-QD overlap, the inter-QD couplings they induce

†Corresponding author. E-mail: wang-yijie@pku.edu.cn
‡Corresponding author. E-mail: songzd@pku.edu.cn

© 2025 Chinese Physical Society and IOP Publishing Ltd. All rights, including for text and data mining, AI training, and similar technologies, are reserved.

must be exponentially small in $a_{\rm M}/\xi$. On the contrary, the direct Coulomb interactions take the form of multipole moment interactions, hence decay in powers of $\xi/a_{\rm M}$. Therefore, the direct Coulomb interaction dominates in the deep moiré potential limit. As the direct Coulomb interaction only acts on the spatial densities, the leading couplings in the effective qudit model will be in the orbital degrees of freedom.

To be concrete, we investigate the SMS with negligible spin–orbit couplings (SOC), and focus on filling $\nu = 3$, where the QD ground states can be 4-fold degenerate, with a 2-fold orbital "qubit" carrying opposite orbital angular momenta $L = \pm 1$, times a 2-fold spin "qubit" with $\zeta = \uparrow, \downarrow$. By neglecting the subleading hopping and exchange Coulomb interactions, we focus on the direct Coulomb interaction that acts on the orbital qubit, and show that for a square lattice with D_4 symmetry, the effective Hamiltonian must be an anisotropic XY model (which includes XX and YY interactions with different amplitudes). We identify the favored orbital order at the mean-field level. For a triangular lattice model with D_6 symmetry, on the other hand, a generalized XY model (which also contains XY interactions) is realized. We show that, at the mean-field level, the energy of all the nearest-neighbor bonds cannot be optimized simultaneously, hence the model is geometrically frustrated.

Finally, we expect that the general principle of designing effective qudit models using the moiré QD array is applicable to more moiré systems, e.g., with strong SOC, or with non-parabolic low-energy dispersions such as graphenes. The effects of the subleading hopping and exchange Coulomb interaction are also discussed.

2. Semiconductor moiré superlattices

For simplicity, we consider a semiconductor band with an isotropic effective mass m subject to a cosine moiré potential.[21,25] Assuming no SOC at this stage, we have the free Hamiltonian

$$H_0 = \sum_\zeta \int \mathrm{d}^2\boldsymbol{r}\, \psi^\dagger_\zeta(\boldsymbol{r}) H_0(\boldsymbol{r}) \psi_\zeta(\boldsymbol{r}),$$

$$H_0(\boldsymbol{r}) = -\frac{\hbar^2}{2m}\nabla^2_{\boldsymbol{r}} - V\sum_{i=1}^{n} \cos(\boldsymbol{G}_i\cdot\boldsymbol{r}), \tag{1}$$

where $\psi^\dagger_\zeta(\boldsymbol{r})$ creates an electron with spin $\zeta = \uparrow, \downarrow$ at $\boldsymbol{r}$. $V > 0$ measures the moiré potential strength, and $\boldsymbol{G}_i$ $(i = 1, \ldots, n)$ are moiré reciprocal lattice vectors depending on the lattice type. For a square lattice, $n = 4$, $\boldsymbol{G}_1 = \frac{2\pi}{a_{\rm M}}(1,0)$, and for a triangular lattice, $n = 6$, and $\boldsymbol{G}_1 = \frac{4\pi}{\sqrt{3}a_{\rm M}}(1,0)$. Other $\boldsymbol{G}_i$ vectors can be generated by spatial rotation, $\boldsymbol{G}_i = C_{nz}^{i-1}\boldsymbol{G}_1$. We also denote the positions of the periodic minima of the moiré potential as $\boldsymbol{R}$. Besides Eq. (1), the SMS is also subject to a chemical potential that fixes the total filling. The electrons are also subject to a long-range Coulomb repulsion,

$$H_{\rm int} = \sum_{\zeta,\zeta'} \frac{1}{2}\int \mathrm{d}^2\boldsymbol{r}\,\mathrm{d}^2\boldsymbol{r}'\, \psi^\dagger_\zeta(\boldsymbol{r})\psi^\dagger_{\zeta'}(\boldsymbol{r}') \times U(\boldsymbol{r}-\boldsymbol{r}')\psi_{\zeta'}(\boldsymbol{r}')\psi_\zeta(\boldsymbol{r}). \tag{2}$$

Here, we take $U(\boldsymbol{r}-\boldsymbol{r}') = \frac{e^2}{\epsilon|\boldsymbol{r}-\boldsymbol{r}'|}$,[21,22] where $\epsilon = \epsilon_0\epsilon_{\rm r}$ and $\epsilon_{\rm r}$ is the dielectric constant. Due to the absence of SOC, the SMS model (including Eqs. (1) and (2)) is invariant under the global spin $SU(2)_\zeta$ (subscript ζ denotes spin, distinguished from subscript L for angular momentum) rotation, and the orbital part obeys the (spinless) wallpaper group $P4mm$ ($P6mm$) for the square and triangular lattices, respectively. Without external magnetic fields, the SMS also enjoys Kramer's time-reversal symmetry $\mathcal{T}$, which can be combined with a spin π-rotation to generate the spinless time-reversal symmetry ($\mathcal{T}^2 = 1$).

When the periodic potential dominates over the kinetic energy, $V \gg \frac{\hbar^2}{2ma_{\rm M}^2}$, the low-energy single-electron wavefunctions will localize at the periodic minima of the potential, forming effective quantum dots. The inter-site hopping becomes negligible, leading to flat single-electron bands with trivial topology. It is thus convenient to work with the Wannier orbitals of these low-energy bands,

$$\psi^\dagger_{\boldsymbol{R}\alpha\zeta} = \int \mathrm{d}^2\boldsymbol{r}\,\psi^\dagger_\zeta(\boldsymbol{r}) w_\alpha(\boldsymbol{r}-\boldsymbol{R}), \tag{3}$$

where α labels the orthonormal Wannier orbitals located at $\boldsymbol{R}$. As the periodic potential is parabolic near each minimum, effectively forming a 2D isotropic harmonic oscillator (HO), we will show in Subsection 2.1 that α for the low-energy bands can be understood as the 2D HO single-particle levels.

On the Wannier basis, the SMS Hamiltonian [Eqs. (1) and (2)] reads

$$H_0 = \sum_{\boldsymbol{R}_1\boldsymbol{R}_2}\sum_{\alpha\beta}\sum_{\zeta} t_{\boldsymbol{R}_1\alpha,\boldsymbol{R}_2\beta}\,\psi^\dagger_{\boldsymbol{R}_1\alpha\zeta}\psi_{\boldsymbol{R}_2\beta\zeta},$$

$$H_{\rm int} = \frac{1}{2}\sum_{\substack{\boldsymbol{R}_1\boldsymbol{R}_2\\ \boldsymbol{R}_3\boldsymbol{R}_4}}\sum_{\alpha\beta\alpha'\beta'}\sum_{\zeta\zeta'} U^{\boldsymbol{R}_1\alpha',\boldsymbol{R}_2\beta'}_{\boldsymbol{R}_3\alpha,\boldsymbol{R}_4\beta} \times \psi^\dagger_{\boldsymbol{R}_1\alpha'\zeta}\psi^\dagger_{\boldsymbol{R}_2\beta'\zeta'}\psi_{\boldsymbol{R}_4\beta\zeta'}\psi_{\boldsymbol{R}_3\alpha\zeta}, \tag{4}$$

where

$$t_{\boldsymbol{R}_1\alpha,\boldsymbol{R}_2\beta} = \int \mathrm{d}^2\boldsymbol{r}\,\omega^*_\alpha(\boldsymbol{r}-\boldsymbol{R}_1)H_0(\boldsymbol{r})\omega_\beta(\boldsymbol{r}-\boldsymbol{R}_2), \tag{5}$$

$$U^{\boldsymbol{R}_1\alpha',\boldsymbol{R}_2\beta'}_{\boldsymbol{R}_3\alpha,\boldsymbol{R}_4\beta} = \int \mathrm{d}^2\boldsymbol{r}_1\int \mathrm{d}^2\boldsymbol{r}_2\,\omega^*_{\alpha'}(\boldsymbol{r}_1-\boldsymbol{R}_1) \times \omega^*_{\beta'}(\boldsymbol{r}_2-\boldsymbol{R}_2)U(\boldsymbol{r}_1-\boldsymbol{r}_2) \times \omega_\beta(\boldsymbol{r}_2-\boldsymbol{R}_4)\omega_\alpha(\boldsymbol{r}_1-\boldsymbol{R}_3) \tag{6}$$

are the hopping and interaction integrals in the Wannier representation. Due to the translation symmetry, the hopping integral $t_{\boldsymbol{R}_1\alpha,\boldsymbol{R}_2\beta}$ will depend on the difference $\boldsymbol{R}_1 - \boldsymbol{R}_2$, rather than $\boldsymbol{R}_1$, $\boldsymbol{R}_2$ separately. And $U^{\boldsymbol{R}_1\alpha',\boldsymbol{R}_2\beta'}_{\boldsymbol{R}_3\alpha,\boldsymbol{R}_4\beta}$ will be independent

of the center of mass coordinates $\boldsymbol{R}_1+\boldsymbol{R}_2+\boldsymbol{R}_3+\boldsymbol{R}_4$. The Wannier orbitals center at the $1a$ Wyckoff positions, which obey the (spinless) point group $4mm$ ($6mm$) for square and triangular lattices, respectively, which are generated by C_{nz} and M_y actions. We work in such a basis that each Wannier orbital α is an eigenstate of the C_{nz} rotation,

$$C_{nz}\psi^\dagger_{\boldsymbol{R}\alpha\zeta}C_{nz}^{-1}=\psi^\dagger_{(C_{nz}\boldsymbol{R})\alpha\zeta}\,\mathrm{e}^{-\mathrm{i}\frac{2\pi}{n}L_\alpha}, \tag{7}$$

where L_α is an integer defined up to n that indicates the angular momentum of orbital α. We also dub the spinless time-reversal counterpart of the α orbital as $\overline{\alpha}$, so that

$$T\psi^\dagger_{\boldsymbol{R}\alpha\zeta}T^{-1}=\psi^\dagger_{\boldsymbol{R}\overline{\alpha}\zeta}. \tag{8}$$

Note that $L_{\overline{\alpha}}=-L_\alpha$ as T reverses the angular momentum. Finally, as in the problem of 2D harmonic oscillators (see Subsection 2.1), we are always able to choose the gauge of the Wannier orbitals so that

$$M_y\psi^\dagger_{\boldsymbol{R}\alpha\zeta}M_y^{-1}=\psi^\dagger_{(M_y\boldsymbol{R})\overline{\alpha}\zeta}. \tag{9}$$

For later convenience, we also introduce Kramer's spinful time-reversal $\mathcal{T}$ that obeys $\mathcal{T}^2=(-1)^F$, where F denotes the fermion parity,

$$\mathcal{T}\psi^\dagger_{\boldsymbol{R}\alpha\zeta}\mathcal{T}^{-1}=\sum_{\zeta'}\psi^\dagger_{\boldsymbol{R}\overline{\alpha}\zeta'}(-\mathrm{i}\sigma_y)_{\zeta'\zeta}. \tag{10}$$

2.1. Single quantum dot

We first focus on the QD at $\boldsymbol{R}$, e.g., $\boldsymbol{R}=0$, hence the $\boldsymbol{R}$ subscripts will be kept implicit unless specified. With the cosine potential expanded to the quadratic order of $|\boldsymbol{r}/a_{\mathrm{M}}|$, the (first-quantized) single-particle Hamiltonian reads

$$H_0(\boldsymbol{r})=-\frac{\hbar^2}{2m}\nabla^2_{\boldsymbol{r}}+\frac{V}{2}\left[Z_n\left(\frac{2\pi}{a_{\mathrm{M}}}\right)^2\right]\boldsymbol{r}^2, \tag{11}$$

up to a constant term that can be absorbed in the chemical potential. Here, $Z_n=2$ for square lattices ($n=4$) and $Z_n=4$ for triangular lattices ($n=6$). Equation (11) corresponds to a 2D harmonic oscillator with frequency $\hbar\omega=\frac{h}{a_{\mathrm{M}}}\sqrt{\frac{Z_nV}{m}}$, with a characteristic spatial expansion $\xi=\sqrt{\frac{\hbar}{m\omega}}=(\frac{a_{\mathrm{M}}\hbar}{\pi})^{1/2}(\frac{1}{4Z_nmV})^{1/4}$. In Eq. (11), the parabolic potential is isotropic, thus the QD enjoys a continuous $SO(2)_L$ rotation symmetry around the z-axis. The angular momentum operator can be correspondingly defined as $\hat{L}=x(-\mathrm{i}\hbar\partial_y)-y(-\mathrm{i}\hbar\partial_x)$. Note that, higher order expansions generically break $SO(2)_L$ to the realistic discrete C_{nz} symmetries, but do not split the $L=\pm1$ states, as they are still protected by M_y.

We first focus on the solution of the 2D harmonic oscillators, which serves as the single particle basis in our problem. Define two groups of ladder operators $\hat{a}_\pm=\frac{1}{2}\left(\frac{x\mp\mathrm{i}y}{\xi}+\xi(\partial_x\mp\mathrm{i}\partial_y)\right)$. Then $\hat{n}_\pm=a^\dagger_\pm a_\pm$ will be two commuting operators with non-negative integer eigenvalues, $n_\pm=0,1,\ldots$. The single-particle Hamiltonian is expressed as

$$H_0(\boldsymbol{r})=\hbar\omega(\hat{n}_++\hat{n}_-+1), \tag{12}$$

and the angular momentum reads

$$\hat{L}=\hbar(\hat{n}_+-\hat{n}_-). \tag{13}$$

By defining $N=n_++n_-$, all the single-particle levels can be labeled in one-to-one correspondence by $N=0,1,\ldots$ and $L=-|N|,-|N|+2,\ldots,|N|-2,|N|$, as shown in Fig. 1.

Notably, the degeneracy of all single-particle levels of the same N is protected by an enlarged symmetry group $SU(2)_L\supset SO(2)_L$, which is generated by $\hat{L}$, $\hbar\hat{a}^\dagger_+\hat{a}_-$, and $\hbar\hat{a}^\dagger_-\hat{a}_+$. The degeneracy from the lowest energy levels to higher is $N+1=1,2,3,\ldots$, respectively. We denote the s-orbital as $(N,L)=(0,0)$, and the p$_\pm$-orbitals as $(N,L)=(1,\pm1)$, respectively. The wave-functions of each level can be chosen as[21]

$$\begin{aligned}\omega_{(N,L)}(\boldsymbol{r}) &= \frac{(-1)^{\frac{N-|L|}{2}}}{\xi}\sqrt{\frac{(\frac{N-|L|}{2})!}{\pi(\frac{N+|L|}{2})!}}\times\mathrm{e}^{\mathrm{i}L\theta}(r/\xi)^{|L|}\\ &\quad\times L^{|L|}_{\frac{N-|L|}{2}}((r/\xi)^2)\times\mathrm{e}^{-\frac{(r/\xi)^2}{2}},\end{aligned} \tag{14}$$

where r and θ represent the length and azimuthal angle of $\boldsymbol{r}$, and $L^{|L|}_{\frac{N-|L|}{2}}$ is the generalized Laguerre polynomial. For both the s-orbital with $(N,L)=(0,0)$ and the p-orbitals with $(N,L)=(1,\pm1)$, the generalized Laguerre polynomials are trivial, $L^0_0(x)=L^1_0(x)=1$.

In adjacent QDs, as the overlap between the low-energy single-particle levels will be exponentially small ($\sim\ \mathrm{e}^{-\frac{(a_{\mathrm{M}}/\xi)^2}{2}}$), the Wannier orbitals can be well approximated by the 2D HO wave-functions Eq. (14). We henceforth denote $\alpha=(N_\alpha,L_\alpha)$. It can be directly verified that equation (14) realizes the gauge-fixing of the symmetry representations Eqs. (7)–(9).

Within the single-particle basis Eq. (14), the full QD Hamiltonian takes the following form:

$$\begin{aligned}H &= \sum_\alpha\sum_\zeta(\hbar\omega(N_\alpha+1))\psi^\dagger_{\alpha\zeta}\psi_{\alpha\zeta}\\ &\quad+\frac{1}{2}\sum_{\alpha\beta\alpha'\beta'}\sum_{\zeta\zeta'}U^{\alpha'\beta'}_{\alpha\beta}\psi^\dagger_{\alpha'\zeta}\psi^\dagger_{\beta'\zeta'}\psi_{\beta\zeta'}\psi_{\alpha\zeta},\end{aligned} \tag{15}$$

where $U^{\alpha'\beta'}_{\alpha\beta}$ is given by Eq. (6). In particular, $U^{\mathrm{ss}}_{\mathrm{ss}}=\frac{e^2}{\epsilon\xi}\sqrt{\frac{\pi}{2}}$ serves as a characterization scale of the on-site repulsion, and we introduce the dimensionless parameter $\lambda_{\mathrm{C}}=U^{\mathrm{ss}}_{\mathrm{ss}}/(\hbar\omega)$ to characterize its relative strength to the 2D HO frequency. We treat λ_{C} as the second tunable parameter, as the overall strength of the Coulomb interaction can vary with the relative screening ϵ_{r}.

Without interaction, electrons fill the single-particle levels sequentially. We especially focus on $\nu = 3$, which is the lowest filling with ground state degeneracy. The many-body ground states are 4-fold degenerate, with a 2-fold spin degeneracy and a 2-fold orbital degeneracy (Fig. 1),

$$|L,\zeta\rangle = \psi^{\dagger}_{(1,L)\zeta}\psi^{\dagger}_{s\uparrow}\psi^{\dagger}_{s\downarrow}|0\rangle\,, \tag{16}$$

where $L = \pm 1$ and $\zeta = \uparrow,\downarrow$, and $|0\rangle$ is the vacuum. The first excited states are separated by an energy gap of $\hbar\omega$, which are 18-fold degenerate, corresponding to moving the p-orbital electron (6-fold) or the s-orbital electron (12-fold) to one level above. With interaction gradually turned on, the many-body levels are perturbed. Importantly, since the interaction does not obey the enlarged $SU(2)_L$ symmetry, accidental degeneracies among excited states will be removed. However, the four ground states remain degenerate, as the orbital degeneracy of $L = \pm$ is protected by point group $4mm$ ($6mm$), while spin degeneracy $\zeta = \uparrow,\downarrow$ is protected by spin $SU(2)_\zeta$.

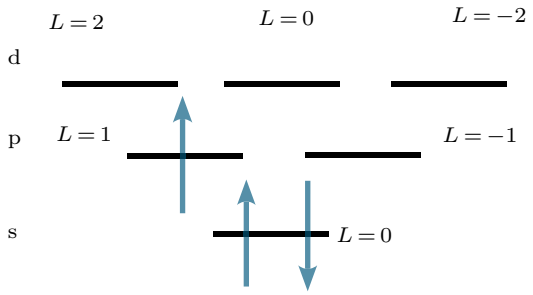


Fig. 1. The ground state configuration of three electrons in the non-interaction limit.

It is important to examine whether the many-body gap remains large with finite interaction. On the one hand, the excitation energy to $\nu = 2$ and $\nu = 4$ sectors can be estimated as on the order of $\Delta_2 = \hbar\omega$ and $\Delta_4 = \lambda_C\hbar\omega$, respectively. On the other hand, the excitation energy within the $\nu = 3$ sector is obtained by direct diagonalization, and plotted in Fig. 2. We find that the gap to the ground states Δ decreases with λ_C, and becomes weak ($\Delta \lesssim 0.1\hbar\omega$) for $\lambda_C \gtrsim 2.4$, which is shown in Fig. 2(a). Therefore, we define $\hbar\omega_\star = \min\{\Delta_2, \Delta, \Delta_4\}$ to characterize the overall many-body gap. It is thus desirable for λ_C to be around 1.0, where the strength of the Coulomb interaction is moderate, and there is a sufficient energy gap between the ground state and the first excited state. We also note that, for $\lambda_C = 1.0$, the non-interacting ground states Eq. (16) remain the dominating component of the interacting ground states ($\approx 90\%$). For a realistic second-order multi-scale system (SMS), such as twisted transition metal dichalcogenides (tTMD), we consider parameters $m = 0.2m_e$, $a_M = 15$ nm, and $\epsilon_r = 5$[23] to simulate realistic systems like $WSe_2/MoSe_2$ and WSe_2/WS_2.[25,26] We vary the potential V from 30 meV to 80 meV and calculate the ratio of the 2D harmonic oscillator characteristic length to the lattice constant, given by ξ/a_M. The behaviors of ξ/a_M and λ_C are illustrated in Fig. 2(b).

Finally, we fix the representation of the (spinless) crystalline and time-reversal symmetries on the many-body ground states the same as the non-interacting one Eq. (16). They are characterized by the following 2×2 matrices:

$$[D(g)]_{L',L} = \langle L',\zeta;g\boldsymbol{R}|g|L,\zeta;\boldsymbol{R}\rangle, \tag{17}$$

which is a linear map from the orbital degrees of freedom at site $\boldsymbol{R}$ to those at $\boldsymbol{R}' = g\boldsymbol{R}$. It can be directly verified from Eqs. (7)–(9) that the non-interacting ground states Eq. (16) satisfy

$$D(M_y) = X, \tag{18}$$

$$D(C_{nz}) = e^{-i\frac{2\pi}{n}Z}, \tag{19}$$

$$D(T) = X. \tag{20}$$

Here, $1, X, Y, Z$ denote the identity and Pauli matrices on the orbital degrees of freedom.

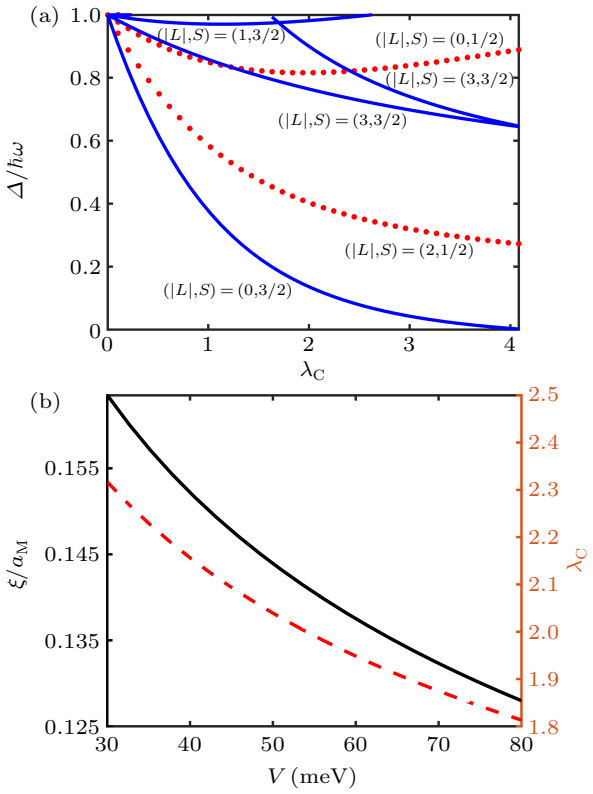


Fig. 2. (a) The evolution of the energy gap $\Delta/(\hbar\omega)$ between the excited states and ground states with λ_C. These states are labeled by $(|L|,S)$. (b) The evolution of ξ/a_M and $\lambda_C = U^{ss}_{ss}/(\hbar\omega)$ for square lattice when moiré potential V varies from 30 meV to 80 meV, with parameters $m = 0.2m_e$, $a_M = 15$ nm, and $\epsilon_r = 5$.

2.2. Inter-quantum-dot couplings

On the original lattice, for an energy scale lower than $\hbar\omega_\star$, it suffices to include the ground states of each QD at $\boldsymbol{R}$, which we dub as $|L,\zeta\rangle_{\boldsymbol{R}}$. We now analyze the scaling behavior of various inter-QD couplings in the limit of $V \gg \frac{\hbar^2}{2ma_M^2}$.

To begin with, according to Eq. (5), inter-site hopping elements $t_{\boldsymbol{R}\alpha,\boldsymbol{R}'\beta}$ involve an overlap of the two Wannier functions, which is exponentially small. To be concrete, the Gaussian factors in the product of $w^*_\alpha(\boldsymbol{r})$ and $w_\alpha(\boldsymbol{r}-\boldsymbol{R})$ can be

written as

$$\mathrm{e}^{-\frac{|\boldsymbol{r}|^2}{2\xi^2}}\mathrm{e}^{-\frac{|\boldsymbol{r}-\boldsymbol{R}|^2}{2\xi^2}}=\mathrm{e}^{-\frac{|\boldsymbol{r}-\frac{\boldsymbol{R}}{2}|^2}{\xi^2}}\mathrm{e}^{-\frac{R^2}{4\xi^2}}, \tag{21}$$

which is upper bounded by the exponentially small factor $\mathrm{e}^{-\frac{R^2}{4\xi^2}}$. The hopping t can be much smaller than on-site U in the limit of $V\gg\frac{h^2}{2ma_{\mathrm{M}}^2}$, which has the ξ dependence as $\mathrm{e}^{-\frac{R^2}{\xi^2}}$ and $1/\xi$, respectively. Since the inter-site hopping changes the on-site occupation, it does not induce perturbative couplings in the low-energy space at the first order of hopping. By inducing virtual processes that exchange an electron between adjacent sites, a super-exchange can be induced at the second order of hopping. As a second order process, the super-exchange amplitude must also decay exponentially as $\mathrm{e}^{-\frac{R^2}{2\xi^2}}$. Next, we examine the Coulomb interactions. For inter-site interaction in the low energy space, there must be either $\boldsymbol{R}_1=\boldsymbol{R}_3$, $\boldsymbol{R}_2=\boldsymbol{R}_4$, which we term as the direct interaction, or $\boldsymbol{R}_1=\boldsymbol{R}_4$, $\boldsymbol{R}_2=\boldsymbol{R}_3$, which we term as the exchange interaction. The exchange interaction elements are given by

$$\begin{aligned}J^{\alpha'\beta'}_{\alpha\beta}(\boldsymbol{R})&=U^{\boldsymbol{R}\alpha',\boldsymbol{0}\beta'}_{\boldsymbol{0}\alpha,\boldsymbol{R}\beta}\\&=\int\mathrm{d}^2\boldsymbol{r}_1\int\mathrm{d}^2\boldsymbol{r}_2\omega^*_{\alpha'}(\boldsymbol{r}_1-\boldsymbol{R})\omega_\alpha(\boldsymbol{r}_1)\\&\quad\times\frac{e^2}{\epsilon|\boldsymbol{r}_1-\boldsymbol{r}_2|}\times\omega^*_{\beta'}(\boldsymbol{r}_2)\omega_\beta(\boldsymbol{r}_2-\boldsymbol{R}),\end{aligned} \tag{22}$$

which also involves the overlap of Wannier functions at different sites, $\omega^*_{\alpha'}(\boldsymbol{r}_1-\boldsymbol{R})\omega_\alpha(\boldsymbol{r}_1)$ and $\omega^*_{\beta'}(\boldsymbol{r}_2)\omega_\beta(\boldsymbol{r}_2-\boldsymbol{R})$. Similar to the hopping and super-exchange strengths, the exchange interaction elements must also decay exponentially as $\mathrm{e}^{-\frac{R^2}{2\xi^2}}$.

Finally, we turn to the direct interaction elements,

$$\begin{aligned}W^{\alpha'\beta'}_{\alpha\beta}(\boldsymbol{R})&=U^{\boldsymbol{R}\alpha',0\beta'}_{\boldsymbol{R}\alpha,0\beta}\\&=\int\mathrm{d}^2\boldsymbol{r}_1\int\mathrm{d}^2\boldsymbol{r}_2\ \omega^*_{\alpha'}(\boldsymbol{r}_1-\boldsymbol{R})\omega_\alpha(\boldsymbol{r}_1-\boldsymbol{R})\\&\quad\times\frac{\mathrm{e}^2}{\epsilon|\boldsymbol{r}_1-\boldsymbol{r}_2|}\times\omega^*_{\beta'}(\boldsymbol{r}_2)\omega_\beta(\boldsymbol{r}_2).\end{aligned} \tag{23}$$

The integrand is Coulomb repulsion between two charge density profiles $\omega^*_{\alpha'}(\boldsymbol{r}_1)\omega_\alpha(\boldsymbol{r}_1)$ and $\omega^*_{\beta'}(\boldsymbol{r}_2)\omega_\beta(\boldsymbol{r}_2)$ centered at $\boldsymbol{R}$ and $\boldsymbol{0}$, respectively. Since the spatial extension of each charge density distribution is characterized by $\xi\ll a_{\mathrm{M}}$, equation (23) can be computed through the multipole moment decomposition (Appendix A), whose asymptotic behavior scales in the power law $\frac{e^2}{\epsilon R}\left(\frac{\xi}{R}\right)^M$, where the power M is determined by the leading order of multipole moments. For example, if $\alpha=\alpha'$, $\int\mathrm{d}^2\boldsymbol{r}|\omega_\alpha(\boldsymbol{r})|^2=1$, the leading order ($M=0$) will be the total (complex) charge, hence $W^{\alpha\beta}_{\alpha\beta}(\boldsymbol{R})\sim\frac{e^2}{\epsilon|\boldsymbol{R}|}$. However, as will be shown in Sections 3 and 4, these elements only contribute to a constant energy to the subspace of QD ground states, instead of inducing inter-QD couplings. The inter-QD couplings will be induced by matrix elements with the forms of $W^{\mathrm{p}+\mathrm{p}+}_{\mathrm{p}-\mathrm{p}-}(\boldsymbol{R})$ and $W^{\mathrm{p}+\mathrm{p}-}_{\mathrm{p}-\mathrm{p}+}(\boldsymbol{R})$. It can be seen from Eq. (14) that $w^*_{\mathrm{p}+}(\boldsymbol{r})w_{\mathrm{p}-}(\boldsymbol{r})\sim\mathrm{e}^{-\mathrm{i}2\theta}$, which has vanishing total charge, vanishing dipole, but finite quadrupole. The integral corresponds to an interaction between two quadrupoles, which scales as $\frac{e^2}{\epsilon|\boldsymbol{R}|}\left(\frac{\xi}{R}\right)^4$. Thus, in the considered limit of $V\gg\frac{h^2}{2ma_{\mathrm{M}}^2}$, $\xi\ll a_{\mathrm{M}}$, the direct interaction elements dominate over the hopping elements and the exchange interaction elements, which decay exponentially with (a_{M}/ξ).

For the parameters presented in Subsection 2.1, we estimate the nearest neighbor elements $W^{\mathrm{p}+\mathrm{p}+}_{\mathrm{p}-\mathrm{p}-}(\boldsymbol{R})$ and $W^{\mathrm{p}+\mathrm{p}-}_{\mathrm{p}-\mathrm{p}+}(\boldsymbol{R})$. In comparison, $J^{\mathrm{ss}}_{\mathrm{ss}}(\boldsymbol{R})$ and $J^{\mathrm{p}+\mathrm{p}-}_{\mathrm{p}-\mathrm{p}+}(\boldsymbol{R})$ are plotted in Fig. 3. When V varies from 30 meV to 80 meV, $J^{\mathrm{ss}}_{\mathrm{ss}}(\boldsymbol{R})$ and $J^{\mathrm{p}+\mathrm{p}-}_{\mathrm{p}-\mathrm{p}+}(\boldsymbol{R})$ decay faster than $W^{\mathrm{p}+\mathrm{p}+}_{\mathrm{p}-\mathrm{p}-}(\boldsymbol{R})$ and $W^{\mathrm{p}+\mathrm{p}-}_{\mathrm{p}-\mathrm{p}+}(\boldsymbol{R})$. And the condition $W^{\mathrm{p}+\mathrm{p}+}_{\mathrm{p}-\mathrm{p}-}(\boldsymbol{R})>W^{\mathrm{p}+\mathrm{p}-}_{\mathrm{p}-\mathrm{p}+}(\boldsymbol{R})$ is satisfied.

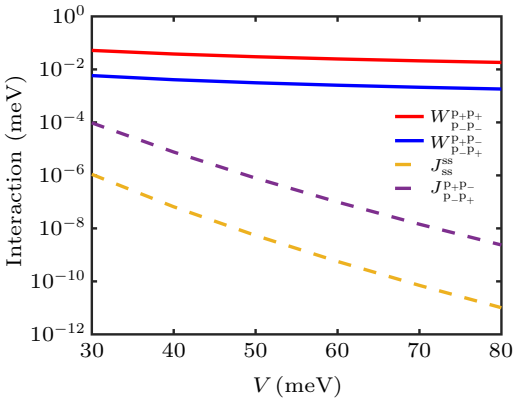


Fig. 3. The nearest interaction elements $W^{\mathrm{p}+\mathrm{p}+}_{\mathrm{p}-\mathrm{p}-}(a_{\mathrm{M}})$, $W^{\mathrm{p}+\mathrm{p}-}_{\mathrm{p}-\mathrm{p}+}(a_{\mathrm{M}})$, $J^{\mathrm{ss}}_{\mathrm{ss}}(a_{\mathrm{M}})$ and $J^{\mathrm{p}+\mathrm{p}-}_{\mathrm{p}-\mathrm{p}+}(a_{\mathrm{M}})$ as a function of moiré potential V. The parameters chosen are the same as those in Fig. 2(b).

For later convenience, we re-write the direct interaction as follows:

$$H_{\mathrm{d}}=\frac{1}{2}\sum_{\boldsymbol{R}\boldsymbol{R}'}\sum_{\alpha\beta\alpha'\beta'}\rho_{\alpha',\alpha}(\boldsymbol{R})W^{\alpha'\beta'}_{\alpha\beta}(\boldsymbol{R}-\boldsymbol{R}')\rho_{\beta',\beta}(\boldsymbol{R}'), \tag{24}$$

and $\rho_{\alpha',\alpha}(\boldsymbol{R})=\sum_\zeta\psi^\dagger_{\boldsymbol{R}\alpha'\zeta}\psi_{\boldsymbol{R}\alpha\zeta}$ can be understood as a component of the total density operator projected to the Wannier basis. Consequently, H_{d} only acts on the orbital degrees of freedom, while preserving the $SU(2)_\zeta$ symmetry at each site. Sections 3 and 4 investigate the effective model H_{d} on the orbital degrees of freedom, it suffices to keep track of one spin species, e.g., $\zeta=\uparrow$. For simplicity, we dub the basis states of the remaining orbital degrees of freedom, the orbital "qubit", as $|L\rangle_{\boldsymbol{R}}$, with $L=\pm$. In experiments, spins can also be polarized by applying a strong in-plane magnetic field.

3. Anistropic *XY* model on square lattices

In this section, we consider a square lattice, and focus on the nearest-neighbor couplings. Further-neighbor couplings are neglected, as they decay with a high power $(\xi/R)^4$. We show that, dictated by the crystalline *P*4*mm* and time-reversal

symmetries, the effective model for the orbital degrees of freedom must be an anisotropic XY model

$$H = \sum_{\langle \boldsymbol{R},\boldsymbol{R}'\rangle} h_{xx} X_{\boldsymbol{R}} X_{\boldsymbol{R}'} + h_{yy} Y_{\boldsymbol{R}} Y_{\boldsymbol{R}'}. \tag{25}$$

In general, the coupling can take any form of $h_{ab}(\boldsymbol{R}) A_{\boldsymbol{0}} B_{\boldsymbol{R}}$, where $A,B = 1,X,Y,Z$ represent the identity and Pauli matrices for the orbital degree of freedom. $h_{ab}(\boldsymbol{R})$ is real so that the Hamiltonian is Hermitian, but may depend on the bond orientation in general. While $1_{\boldsymbol{0}} 1_{\boldsymbol{R}}$ merely contributes a constant energy, hence can be ignored, $1_{\boldsymbol{0}} B_{\boldsymbol{R}}$ and $A_{\boldsymbol{0}} 1_{\boldsymbol{R}}$ ($A,B \neq 1$) represent a Zeeman field imposed on the qubit at $\boldsymbol{R}$ or $\boldsymbol{0}$ by the bond, and $A_{\boldsymbol{0}} B_{\boldsymbol{R}}$ ($A,B \neq 1$) represent interactions. For a horizontal bond that respects the M_y and T symmetries, $A_{\boldsymbol{0}} B_{\boldsymbol{R}}$ must commute with both $D(M_y) \otimes D(M_y)$ and $D(T) \otimes D(T) K$, where K represents the complex conjugation, with $D(M_y)$ and $D(T)$ given by Eqs. (18) and (20). Consequently, only the following terms can survive for $\boldsymbol{R} = R\hat{e}_x$:

$$\begin{aligned} H_{\langle \boldsymbol{0},\boldsymbol{R}\rangle} &= h_{x0}(\boldsymbol{R}) X_{\boldsymbol{0}} + h_{0x}(\boldsymbol{R}) X_{\boldsymbol{R}} + h_{xx}(\boldsymbol{R}) X_{\boldsymbol{0}} X_{\boldsymbol{R}} \\ &\quad + h_{yy}(\boldsymbol{R}) Y_{\boldsymbol{0}} Y_{\boldsymbol{R}} + h_{zz}(\boldsymbol{R}) Z_{\boldsymbol{0}} Z_{\boldsymbol{R}}. \end{aligned} \tag{26}$$

On the other hand, the couplings on the vertical bonds should be equal to C_{4z} rotation of the horizontal bonds. Supposing that $\boldsymbol{R}' = C_{4z}\boldsymbol{R}$, by Eq. (19), the coupling for $\boldsymbol{R}' = R\hat{e}_y$ is

$$\begin{aligned} H_{\langle \boldsymbol{0},\boldsymbol{R}'\rangle} &= (-Z\otimes Z) H_{\langle \boldsymbol{0},\boldsymbol{R}\rangle} (-Z\otimes Z) \\ &= -h_{x0}(\boldsymbol{R}) X_{\boldsymbol{0}} - h_{0x}(\boldsymbol{R}) X_{\boldsymbol{R}'} + h_{xx}(\boldsymbol{R}) X_{\boldsymbol{0}} X_{\boldsymbol{R}'} \\ &\quad + h_{yy}(\boldsymbol{R}) Y_{\boldsymbol{0}} Y_{\boldsymbol{R}'} + h_{zz}(\boldsymbol{R}) Z_{\boldsymbol{0}} Z_{\boldsymbol{R}'}. \end{aligned} \tag{27}$$

In particular, the vertical bond must contribute a Zeeman field to the site $\boldsymbol{0}$ that is opposite to the horizontal bond. Therefore, the net Zeeman field at each site must be zero, and only the interaction terms can survive. By Eq. (27), we also find that the interaction coefficients must be the same on both horizontal and vertical bonds.

Finally, we explain that due to the density–density structure, the crystalline symmetries further forbid the ZZ interactions. To see this, we first note that

$$W^{\alpha'\beta'}_{\alpha\beta}(\boldsymbol{R}) = W^{\alpha'\overline{\beta}}_{\alpha\overline{\beta'}}(\boldsymbol{R}) = W^{\overline{\alpha}\beta'}_{\overline{\alpha'}\beta}(\boldsymbol{R}), \tag{28}$$

as $\omega^*_{\beta}(\boldsymbol{r}) = \omega_{\overline{\beta}}(\boldsymbol{r})$ according to Eq. (14), hence $\omega^*_{\beta'}(\boldsymbol{r})\omega_{\beta}(\boldsymbol{r})$ and $\omega^*_{\overline{\beta}}(\boldsymbol{r})\omega_{\overline{\beta'}}(\boldsymbol{r})$ correspond to the same (complex) charge distribution. Therefore, by abbreviating $|LL'\rangle = |L;\boldsymbol{R}\rangle \otimes |L';\boldsymbol{0}\rangle$, there is

$$\begin{aligned} \langle LL'|H_{\rm d}|LL'\rangle &= \sum_{\alpha\beta\alpha'\beta'} \langle L;\boldsymbol{R}|\rho_{\alpha',\alpha}(\boldsymbol{R})|L;\boldsymbol{R}\rangle \times W^{\alpha'\beta'}_{\alpha\beta}(\boldsymbol{R}) \\ &\quad \times \langle L';\boldsymbol{0}|\rho_{\beta',\beta}(\boldsymbol{0})|L';\boldsymbol{0}\rangle. \end{aligned} \tag{29}$$

Due to the time-reversal symmetry, it can be verified that

$$\begin{aligned} \langle \overline{L};\boldsymbol{R}|\rho_{\overline{\beta},\overline{\beta'}}(\boldsymbol{R})|\overline{L};\boldsymbol{R}\rangle &= \langle TL;\boldsymbol{R}|(T\rho_{\beta',\beta}(\boldsymbol{R})T^{-1})^\dagger|TL;\boldsymbol{R}\rangle \\ &= \langle L;\boldsymbol{R}|\rho_{\beta',\beta}(\boldsymbol{R})|L;\boldsymbol{R}\rangle. \end{aligned} \tag{30}$$

Here we use $\langle T\mu|(TAT^{-1})^\dagger|T\alpha\rangle = \langle\alpha|A|\mu\rangle$ and $T\rho_{\beta,\beta'}T^{-1} = \rho_{\overline{\beta},\overline{\beta'}}$. By inserting Eqs. (28) and (30) to Eq. (29), it is thus straightforward to show that

$$\langle +-|H_{\rm d}|+-\rangle = \langle ++|H_{\rm d}|++\rangle, \tag{31}$$

which implies the absence of ZZ interactions. As there are no symmetry constraints that relate the XX and YY interactions, h_{xx} and h_{yy} are in general independent. Therefore, the effective model takes the form of an anisotropic XY model, as in Eq. (25).

Since the interacting ground states at around $\lambda_{\rm C} = 1.0$ can be well approximated ($\approx 90\%$ overlap) by the non-interacting Eq. (16). Let us estimate h_{xx} and h_{yy} with the latter wavefunctions, where they take the following simple form:

$$h_{xx} = \frac{W_1 + W_2}{2} = 0.0123 \text{ meV}, \tag{32}$$

$$h_{yy} = \frac{W_2 - W_1}{2} = -0.010 \text{ meV}. \tag{33}$$

Here, for brevity, we have renamed $W_1 = W^{\rm p_+p_+}_{\rm p_-p_-}(\boldsymbol{R}) = 0.022$ meV, $W_2 = W^{\rm p_+p_-}_{\rm p_-p_+}(\boldsymbol{R}) = 0.0024$ meV, where $\boldsymbol{R}$ is the horizontal nearest-neighbor bond. Parameters $m = 0.2m_{\rm e}$, $V = 40$ meV and $a_{\rm M} = 15$ nm are used in the estimation. For the qualitative analysis below, such an approximation should be valid, as it does not change the order nor the sign of the coupling parameters.

Since a square lattice with only nearest-neighbor couplings can be biparted, two XY models with opposite signs of h_{xx} and/or h_{yy} are simply related by a gauge transformation — acting a unitary transformation of $X_{\boldsymbol{R}}$ or $Y_{\boldsymbol{R}}$ on one of the two sublattices reverses the sign of h_{yy} and h_{xx}, respectively. We expect the ground state of the anisotropic XY model to adopt orbital order as in the ferromagnetic XY model. To investigate the order type, we assume the ground state to adopt the following product state ansatz, which is also equivalent to a mean-field analysis:

$$|\Psi\rangle = \otimes_{\boldsymbol{R}} |\theta(\boldsymbol{R});\boldsymbol{R}\rangle, \tag{34}$$

where

$$|\theta(\boldsymbol{R});\boldsymbol{R}\rangle = \frac{|+;\boldsymbol{R}\rangle + {\rm e}^{{\rm i}\theta(\boldsymbol{R})}|-;\boldsymbol{R}\rangle}{\sqrt{2}}, \quad \theta(\boldsymbol{R}) \in [0,2\pi) \tag{35}$$

satisfies

$$\langle\theta(\boldsymbol{R});\boldsymbol{R}|X_{\boldsymbol{R}}|\theta(\boldsymbol{R});\boldsymbol{R}\rangle = \cos\theta(\boldsymbol{R}), \tag{36}$$

$$\langle\theta(\boldsymbol{R});\boldsymbol{R}|Y_{\boldsymbol{R}}|\theta(\boldsymbol{R});\boldsymbol{R}\rangle = \sin\theta(\boldsymbol{R}). \tag{37}$$

In the real space, the charge density of the $|\theta(\boldsymbol{R});\boldsymbol{R}\rangle$ state is oriented along the azimuthal angle $\theta/2 \bmod \pi$. To see

this, it suffices to use the approximate many-body wavefunction Eq. (16), and identify that the major density difference is contributed by the $\frac{\psi^\dagger_{p+}+e^{i\theta}\psi^\dagger_{p-}}{\sqrt{2}}$ electron. By Eq. (14), $\langle \boldsymbol{r}|\psi^\dagger_{p\pm}|0\rangle = w_{p\pm}(\boldsymbol{r}) \sim e^{\pm i\varphi}$, where φ is the azimuthal angle of $\boldsymbol{r}$. Therefore, the spatial density contributed by the $p_\pm$ electrons are $|\langle \boldsymbol{r}|\frac{\psi^\dagger_{p+}+e^{i\theta}\psi^\dagger_{p-}}{\sqrt{2}}|0\rangle|^2 \sim |e^{i\varphi}+e^{i\theta}e^{-i\varphi}|^2 \sim \cos^2(\varphi-\frac{\theta}{2})$, which is maximal along $\varphi=\theta/2 \bmod \pi$, and minimal along $\varphi=(\theta+\pi)/2 \bmod \pi$. The charge densities of the $\theta(\boldsymbol{R})=0$ and π states are thus oriented along the x and y-axis, respectively.

For a single bond $\langle \boldsymbol{R},\boldsymbol{R}'\rangle$, the mean-field energy is given by

$$\begin{aligned}\langle\Psi|H_{\langle \boldsymbol{R},\boldsymbol{R}'\rangle}|\Psi\rangle &= \frac{W_2}{2}\cos(\theta(\boldsymbol{R})-\theta(\boldsymbol{R}')) \\ &+\frac{W_1}{2}\cos(\theta(\boldsymbol{R})+\theta(\boldsymbol{R}'))\,, \end{aligned} \tag{38}$$

which is minimized by either of the following two conditions:

$$\theta(\boldsymbol{R})=\pi,\ \ \theta(\boldsymbol{R}')=0 \ \text{ or } \ \theta(\boldsymbol{R})=0,\ \ \theta(\boldsymbol{R}')=\pi. \tag{39}$$

It can be seen that the W_2 term tends to lock the relative orientation between adjacent sites as perpendicular ($\theta(\boldsymbol{R})-\theta(\boldsymbol{R}')=\pi$), while the W_1 term further locks the orientation of each single site as either horizontal or vertical. When put on the lattice, the orbital qubits order as depicted in Fig. 4. Two types of ground states are exhibited in Fig. 4, corresponding to two solutions in Eq. (39). It is seen that the ground state of our anisotropic XY model is similar to that of the isotropic spin-1/2 XY model on a square lattice, forming the Néel order.[27]

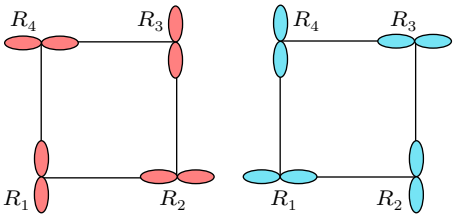


Fig. 4. A schematic illustration of the ground state orbital order of the effective anisotropic XY model on the square lattice.

4. Frustrated generalized XY model on triangular lattices

In this section, we consider a triangular lattice of the QDs. For a single horizontal bond $\langle \boldsymbol{0},\boldsymbol{R}\rangle$ ($\boldsymbol{R}=R\hat{e}_x$), as it still respects the M_y and T symmetries, only terms $1_{\boldsymbol{0}}1_{\boldsymbol{R}}$, $X_{\boldsymbol{0}}1_{\boldsymbol{R}}$, $1_{\boldsymbol{0}}X_{\boldsymbol{R}}$, $X_{\boldsymbol{0}}X_{\boldsymbol{R}}$, $Y_{\boldsymbol{0}}Y_{\boldsymbol{R}}$ and $Z_{\boldsymbol{0}}Z_{\boldsymbol{R}}$ can survive, as explained in Eq. (26) of Section 3. Moreover, due to the symmetry properties of the direct interaction H_d shown in Eq. (31), $Z_{\boldsymbol{0}}Z_{\boldsymbol{R}}$ terms will vanish as well. On the other hand, the couplings on the bond $\langle \boldsymbol{0},C^j_{6z}\boldsymbol{R}\rangle$ ($j=1,2,\ldots 5$) will be determined by a C^j_{6z} conjugation on the horizontal bonds. Supposing $\boldsymbol{R}_{j+1}=C^j_{6z}\boldsymbol{R}$, by Eq. (19), the coupling reads

$$\begin{aligned}H_{\langle 0,\boldsymbol{R}_{j+1}\rangle} &= \left(e^{-i\frac{j\pi}{3}Z}\otimes e^{-i\frac{j\pi}{3}Z}\right)H_{\langle 0,\boldsymbol{R}\rangle}\left(e^{i\frac{j\pi}{3}Z}\otimes e^{i\frac{j\pi}{3}Z}\right) \\ &= h_{x0}(\boldsymbol{R})\left[\cos\frac{2\pi j}{3}X_{\boldsymbol{0}}+\sin\frac{2\pi j}{3}Y_{\boldsymbol{0}}\right] \\ &+h_{0x}(\boldsymbol{R})\left[\cos\frac{2\pi j}{3}X_{\boldsymbol{R}_j}+\sin\frac{2\pi j}{3}Y_{\boldsymbol{R}_j}\right] \\ &+h_{xx}(\boldsymbol{R})\left[\cos\frac{2\pi j}{3}X_{\boldsymbol{0}}+\sin\frac{2\pi j}{3}Y_{\boldsymbol{0}}\right] \\ &\times\left[\cos\frac{2\pi j}{3}X_{\boldsymbol{R}_j}+\sin\frac{2\pi j}{3}Y_{\boldsymbol{R}_j}\right] \\ &+h_{yy}(\boldsymbol{R})\left[\cos\frac{2\pi j}{3}Y_{\boldsymbol{0}}-\sin\frac{2\pi j}{3}X_{\boldsymbol{0}}\right] \\ &\times\left[\cos\frac{2\pi j}{3}Y_{\boldsymbol{R}_j}-\sin\frac{2\pi j}{3}X_{\boldsymbol{R}_j}\right]. \end{aligned} \tag{40}$$

It can be verified that, similar to Section 3, the coefficients of the Zeeman terms, $X_{\boldsymbol{0}}$ and $X_{\boldsymbol{R}}$, will be zero after summing over the six bonds connected to site $\boldsymbol{0}$ ($\boldsymbol{R}$), because $\sum_{j=1}^6 D(C_{6z})^{(j-1)}XD(C_{6z})^{-(j-1)}=0$. Therefore, only the interacting terms remain, which take the form of

$$\begin{aligned}H &= \frac{W_1}{2}\sum_{j=1}^{6}\sum_{\langle \boldsymbol{R},\boldsymbol{R}'\rangle_j}\left[-\sin\left(\frac{2\pi(j-1)}{3}\right)(X_{\boldsymbol{R}}Y_{\boldsymbol{R}'}+Y_{\boldsymbol{R}}X_{\boldsymbol{R}'})\right. \\ &\left.+\cos\left(\frac{2\pi(j-1)}{3}\right)(X_{\boldsymbol{R}}X_{\boldsymbol{R}'}-Y_{\boldsymbol{R}}Y_{\boldsymbol{R}'})\right] \\ &+\frac{W_2}{2}\sum_{\langle \boldsymbol{R},\boldsymbol{R}'\rangle}\left[X_{\boldsymbol{R}}X_{\boldsymbol{R}'}+Y_{\boldsymbol{R}}Y_{\boldsymbol{R}'}\right]. \end{aligned} \tag{41}$$

Here, we have again estimated the coupling parameters using the non-interacting states Eq. (16). $\langle \boldsymbol{R},\boldsymbol{R}'\rangle_j$ ($j=1,\ldots,6$) denotes a nearest bond with orientation angle $(\pi/3)(j-1)$, and $\langle \boldsymbol{R},\boldsymbol{R}'\rangle$ denotes all nearest bonds.

To demonstrate the geometric frustration, let us consider one triangle with vertices $\boldsymbol{R}_{1,2,3}$ first, as illustrated in Fig. 5, and analyze at the mean-field level using the ansatz Eqs. (34) and (35). For brevity, we dub $\theta_{1,2,3}=\theta(\boldsymbol{R}_{1,2,3})$. The optimal configuration for a single horizontal bond $\langle \boldsymbol{R}_1,\boldsymbol{R}_2\rangle$ will be the same as Eq. (39), and the optimal configuration for the $\langle \boldsymbol{R}_1,\boldsymbol{R}_3\rangle$ and $\langle \boldsymbol{R}_2,\boldsymbol{R}_3\rangle$ bonds can be obtained by C_{6z} rotations. It is thus clear that the optimal configuration cannot be achieved for all the three bonds simultaneously, which is a manifestation of the geometric frustration. We can also solve the lowest-energy configuration for one triangle. The mean-field energy is given by

$$\begin{aligned}E &= \sum_{i=1}^{3}\langle\Psi|H_{\langle \boldsymbol{R}_i,\boldsymbol{R}_{i+1}\rangle}|\Psi\rangle \\ &= \frac{W_2}{2}\sum_i\cos(\theta_i-\theta_{i+1}) \\ &+\frac{W_1}{2}\sum_i\cos\left(\theta_i+\theta_{i+1}+\frac{4\pi(i-1)}{3}\right), \end{aligned} \tag{42}$$

where $i = 1,2,3 \bmod 3$. As $W_{1,2} > 0$, it can be verified that the global minimum is achieved by the following two sets of solutions:

$$\theta_i = -\frac{\pi}{6} + \frac{4\pi}{3}(i+1) \text{ or } \theta_i = \frac{5\pi}{6} + \frac{4\pi}{3}(i+1), \quad (43)$$

with energy $E = -\frac{3}{4}W_2 - \frac{3}{2}W_1$. In particular, if $W_2 = 0$, there will be no frustration in one triangle, as the minima of the three W_1 cosine terms are achieved simultaneously. The W_2 term, however, contains frustration. By rewriting it in the following form, its minimum can be directly read off,

$$\frac{W_2}{4}\left(\left|\sum_i \mathrm{e}^{\mathrm{i}\theta_i}\right|^2 - 3\right) \geq -\frac{3}{4}W_2, \quad (44)$$

which is achieved by Eq. (43).

When more than one triangle is considered, the situation will be further complicated, as the optimal mean-field configuration for a single triangle (Fig. 5) cannot be tiled into a lattice. It is also an unsolved question whether the quantum ground state of Eq. (41) can be effectively captured within the mean-field level. We leave them to future researches.

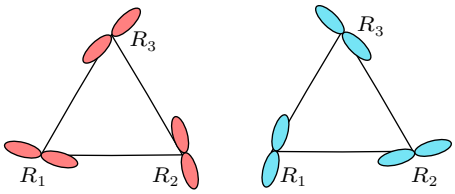


Fig. 5. A schematic illustration of two types of ground state orbital orders of one plaquette of the triangular lattice.

5. Discussion and conclusion

In this work, we have investigated the effective models realized by QD arrays on a SMS with a deep moiré potential. We showed that the direct Coulomb interaction dominates among all inter-QD couplings in such a limit. For the QDs with a two-fold orbital degeneracy with orbital angular momenta $L = \pm 1$ in the ground state manifold, we then demonstrated that various orbital XY models can be realized on the lattice, including an anisotropic XY model on the square lattice, and a geometrically frustrated generalized XY model on the triangle lattice. We emphasize that such a scheme is not restricted to the examples we have studied, but can be applicable more generically. The only input needed is the local qudit space spanned by the QD ground states, and the crystalline symmetries obeyed by the SMS setup. For example, more complicated lattice types may be designed, e.g., honeycomb or kagome, and materials with strong SOC can be explored (Appendix C). It is also interesting to ask whether more exotic QDs can be realized in SMS with non-parabolic dispersions, such as graphene systems.

Finally, we discuss the fate of the remaining spin degrees of freedom of the 4-dimensional qudits. Suppose that the orbital order forms at the energy scale of W, then only an $SU(2)_\zeta$ spin will be left at energy scales below it. Due to the global $SU(2)_\zeta$ symmetry, the coupling must take the form of Heisenberg model $J\sum_{\langle \boldsymbol{R}_1,\boldsymbol{R}_2\rangle} \boldsymbol{S}_{\boldsymbol{R}_1}\cdot\boldsymbol{S}_{\boldsymbol{R}_2}$, where $\boldsymbol{S}$ denotes the $SU(2)_\zeta$ spin generators, and J will only be contributed by the summation of exchange Coulomb interaction, or the super-exchange due to the virtual hoppings. As the energy scale of J is far lower than W, for temperature below $K_W = W/k_\mathrm{B}$, but larger than $K_J = J/k_\mathrm{B}$, the remaining spins will simply behave paramagnetically. While when temperature below $K_J = J/k_\mathrm{B}$, specific spin order forms.

The current work explores how an array of QDs with orbital degeneracy interact in an SMS in a general way, and it remains unknown in which specific system the orbital XY models can be experimentally realized. For the soft cosine moiré potential we have investigated, a deep potential V is required for the formation of QDs, so that inter-QD overlap is exponentially negligible. However, by reducing the QD wave-packet size and hence reducing the quadrupole moment, this condition also suppresses the direct interaction strength, albeit in a power-law manner. For the parameters we have explored, the direct interaction strength has only been found as 10^{-2}–10^{-1} meV, which might be too low for current experiment setups. However, if some steep moiré potential, e.g., periodic square wells, can be designed, then the negligible inter-QD overlap and a considerable wave-packet size can be realized simultaneously. In that case, we expect an orbital XY model to be achievable. Since the moiré potential is typically determined by the local stacking configuration, such a steep moiré potential will generically require a stronger in-plane relaxation, so that sharp domains with different local stacking configurations form.

We also discuss the potential effect of lattice reconstruction. To observe the phenomena associated with the orbital XY models analyzed in our paper, we expect that each structurally stable stacking domain should expand at least tens or hundreds of moiré unit cells, so that the orbital degeneracy of most QDs can be preserved, and adjacent QDs can fully interact to generate the orbital pattern. On the domain wall that separates two stable stacking domains, however, the physics must be analyzed for each concrete material. While the defects or strains on the domain walls may disrupt the crystalline symmetries hence break the orbital degeneracy of the QD ground states, being detrimental to the orbital XY model, it can still be interesting to ask whether new bound states can be trapped at the domain walls, which can interact with the bulk QD array.

Appendix A: Multipole moment expansion

The form of density–density interaction elements $W_{\alpha\beta}^{\alpha'\beta'}(\boldsymbol{R})$ is similar to the Coulomb interaction between two charged bodies, and the difference is that $\rho_{\alpha'\alpha}(\boldsymbol{r})$ and $\rho_{\beta'\beta}(\boldsymbol{r})$ here can be complex numbers. Two 'complex' charges

$\rho(\boldsymbol{r})$ can be calculated by Wannier functions by $\rho_{\alpha'\alpha}(\boldsymbol{r}_1) = \omega^*_{\alpha'}(\boldsymbol{r}_1)\omega_{\alpha}(\boldsymbol{r}_1)$ and $\rho_{\beta'\beta}(\boldsymbol{r}_2) = \omega^*_{\beta'}(\boldsymbol{r}_2)\omega_{\beta}(\boldsymbol{r}_2)$.

$$\begin{aligned} W^{\alpha'\beta'}_{\alpha\beta}(\boldsymbol{R}) &= \frac{e^2}{\epsilon}\int \mathrm{d}^2\boldsymbol{r}_1 \int \mathrm{d}^2\boldsymbol{r}_2 \frac{\rho_{\alpha'\alpha}(\boldsymbol{r}_1)\rho_{\beta'\beta}(\boldsymbol{r}_2)}{|\boldsymbol{r}_2-\boldsymbol{r}_1+\boldsymbol{R}|} \\ &= \frac{e^2}{\epsilon}\int \mathrm{d}^2\boldsymbol{r}_1 \int \mathrm{d}^2\boldsymbol{r}_2 \\ &\quad \times \frac{\rho_{\alpha'\alpha}(\boldsymbol{r}_1)\rho_{\beta'\beta}(\boldsymbol{r}_2)}{\sqrt{(x_2-x_1+R_x)^2+(y_2-y_1+R_y)^2}}. \end{aligned} \tag{A1}$$

Here, we consider two elements $W^{\mathrm{p+p+}}_{\mathrm{p-p-}}(\boldsymbol{R})$ and $W^{\mathrm{p+p-}}_{\mathrm{p-p+}}(\boldsymbol{R})$, with $\rho_{\mathrm{p+p-}}(\boldsymbol{r}) = r^2\mathrm{e}^{-2\mathrm{i}\theta}\mathrm{e}^{-\frac{r^2}{\xi^2}}$ and $\rho_{\mathrm{p-p+}}(\boldsymbol{r}) = r^2\mathrm{e}^{2\mathrm{i}\theta}\mathrm{e}^{-\frac{r^2}{\xi^2}}$. In both cases, $\rho(\boldsymbol{r})$ is an even function. And we do analysis under this condition below.

Let $|\boldsymbol{r}_1|, |\boldsymbol{r}_2| \ll |\boldsymbol{R}|$, and do the expansion of $\frac{|\boldsymbol{r}_1|}{|\boldsymbol{R}|}$ and $\frac{|\boldsymbol{r}_2|}{|\boldsymbol{R}|}$ as follows:

$$\begin{aligned} W^{\alpha'\beta'}_{\alpha\beta}(\boldsymbol{R}) &= \frac{e^2}{\epsilon|\boldsymbol{R}|}\int \mathrm{d}^2\boldsymbol{r}_1 \int \mathrm{d}^2\boldsymbol{r}_2 \\ &\quad \times \frac{\rho_{\alpha'\alpha}(\boldsymbol{r}_1)\rho_{\beta'\beta}(\boldsymbol{r}_2)}{\sqrt{1+\frac{2(x_2-x_1)R_x+2(y_2-y_1)R_y}{R^2}+\frac{(x_2-x_1)^2+(y_2-y_1)^2}{R^2}}} \\ &= \frac{e^2}{\epsilon|\boldsymbol{R}|}\int \mathrm{d}^2\boldsymbol{r}_1 \int \mathrm{d}^2\boldsymbol{r}_2 \rho_{\alpha'\alpha}(\boldsymbol{r}_1)\rho_{\beta'\beta}(\boldsymbol{r}_2) \\ &\quad \times\Bigg[1-\frac{1}{2}\Bigg(\frac{2(x_2-x_1)R_x+2(y_2-y_1)R_y}{R^2} \\ &\quad +\frac{(x_2-x_1)^2+(y_2-y_1)^2}{R^2}\Bigg) \\ &\quad +\frac{3}{8}\Bigg(\frac{2(x_2-x_1)R_x+2(y_2-y_1)R_y}{R^2} \\ &\quad +\frac{(x_2-x_1)^2+(y_2-y_1)^2}{R^2}\Bigg)^2\cdots\Bigg]. \end{aligned} \tag{A2}$$

Now define

$$e^{(1)} = \int \mathrm{d}^2\boldsymbol{r}_1 \rho_{\alpha'\alpha}(\boldsymbol{r}_1), \tag{A3}$$

$$d^{(1)}_i = \int \mathrm{d}^2\boldsymbol{r}_1 \rho_{\alpha'\alpha}(\boldsymbol{r}_1) r_{1i}, \tag{A4}$$

$$Q^{(1)}_{ij} = \int \mathrm{d}^2\boldsymbol{r}_1 \rho_{\alpha'\alpha}(\boldsymbol{r}_1)(3r_{1i}r_{1j}-|\boldsymbol{r}|^2\delta_{ij}), \tag{A5}$$

where r_{1i} is the i component of $\boldsymbol{r}_1$, and Wannier labels α, α' have been omitted in $e^{(1)}$, $d^{(1)}_i$ and $Q^{(1)}_{ij}$ for simplicity.

Then,

$$\begin{aligned} W^{\alpha'\beta'}_{\alpha\beta}(\boldsymbol{R}) &= \frac{e^2}{\epsilon}\Bigg[\frac{e^{(1)}e^{(2)}}{|\boldsymbol{R}|}+\frac{e^{(1)}\boldsymbol{d}^{(2)}\cdot\hat{\boldsymbol{R}}-e^{(2)}\boldsymbol{d}^{(1)}\cdot\hat{\boldsymbol{R}}}{|\boldsymbol{R}|^2} \\ &\quad +\frac{\boldsymbol{d}^{(1)}\cdot\boldsymbol{d}^{(2)}-3(\boldsymbol{d}^{(1)}\cdot\hat{\boldsymbol{R}})(\boldsymbol{d}^{(2)}\cdot\hat{\boldsymbol{R}})}{|\boldsymbol{R}|^3} \\ &\quad +\frac{1}{2}\frac{e^{(1)}\boldsymbol{Q}^{(2)}:\hat{\boldsymbol{R}}\hat{\boldsymbol{R}}+e^{(2)}\boldsymbol{Q}^{(1)}:\hat{\boldsymbol{R}}\hat{\boldsymbol{R}}}{|\boldsymbol{R}|^3} \\ &\quad +O\left(\frac{1}{|\boldsymbol{R}|^5}\right)\Bigg]. \end{aligned} \tag{A6}$$

Because $\int \mathrm{d}\theta\,\mathrm{e}^{2\mathrm{i}\theta} = 0$, the 'charge' term $e^{(1)}$ ($e^{(2)}$) is zero. As a result, the first term ('charge–charge interaction') and the fourth term ('charge–quadrupole interaction') vanish. Since $\rho(\boldsymbol{r})$ considered here is an even function, the dipole term d_i also vanishes, as its integrand with respect to the variable r_i is odd. Thus, the second and third expansion terms are both zero. The reason for the vanishing of the term, which scales as $O\left(\frac{1}{|\boldsymbol{R}|^4}\right)$, is also due to the oddness of the integrand in r_i. Therefore, the leading non-zero term scales as $O\left(\frac{1}{|\boldsymbol{R}|^5}\right)$. The specific form of this term is

$$\begin{aligned} &\frac{e^2}{\epsilon|\boldsymbol{R}|}\int \mathrm{d}^2\boldsymbol{r}_1\rho(\boldsymbol{r}_1)\int \mathrm{d}^2\boldsymbol{r}_2\rho(\boldsymbol{r}_2)\Bigg(\frac{3}{8}\frac{(\boldsymbol{r}_2-\boldsymbol{r}_1)^4}{|\boldsymbol{R}|^4} \\ &-\frac{15}{4}\frac{\left((\boldsymbol{r}_2-\boldsymbol{r}_1)\cdot\hat{\boldsymbol{R}}\right)^2(\boldsymbol{r}_2-\boldsymbol{r}_1)^2}{|\boldsymbol{R}|^4} \\ &+\frac{35}{8}\frac{\left((\boldsymbol{r}_2-\boldsymbol{r}_1)\cdot\hat{\boldsymbol{R}}\right)^4}{|\boldsymbol{R}|^4}\Bigg), \end{aligned} \tag{A7}$$

where α, β indices have been omitted for simplicity.

Appendix B: Hatree–Fock mean field calculation

With interaction turned on, N fold degenerate energy levels due to enlarged $SU(2)_L$ symmetry will break into no more than 2-fold. This picture can be obtained from full-symmetric Hartree–Fock (HF) calculation for one single site with three electrons. The mean field Hamiltonian for filling $\nu = 3$ moiré atom with continuous rotation symmetry is as follows:

$$\begin{aligned} H_{\mathrm{MF}} &= \sum_{\alpha\beta}\sum_{\zeta} E_{\alpha\beta}\psi^\dagger_{\alpha\zeta}\psi_{\beta\zeta} \\ &\quad +\sum_{\alpha\beta\alpha'\beta'}\sum_{\zeta\zeta'} U_{\alpha\beta\alpha'\beta'}\Big(\langle\psi^\dagger_{\alpha\zeta}\psi_{\alpha'\zeta}\rangle\psi^\dagger_{\beta\zeta'}\psi_{\beta'\zeta'} \\ &\quad -\langle\psi^\dagger_{\alpha\zeta}\psi_{\beta'\zeta'}\rangle\psi^\dagger_{\beta\zeta'}\psi_{\alpha'\zeta}\Big), \end{aligned} \tag{B1}$$

where $\psi^\dagger_{\alpha\zeta}$ is the field operator with $\alpha = (N_\alpha, L_\alpha)$ denoting 2D harmonic oscillator states and spin ζ. On-site energy $E_{\alpha\beta} = \delta_{N_\alpha,N_\beta}(N_\alpha+1)\hbar\omega$, and on-site Coulomb interaction matrix element is calculated as[21]

$$\begin{aligned} U_{\alpha\beta\alpha'\beta'} &= \int \frac{\mathrm{d}^2\boldsymbol{q}}{(2\pi)^2}\frac{2\pi e^2}{\epsilon|\boldsymbol{q}|} \\ &\quad \times\langle N_\alpha L_\alpha, N_\beta L_\beta|\,\mathrm{e}^{\mathrm{i}\boldsymbol{q}\cdot(\boldsymbol{r}_1-\boldsymbol{r}_2)}|N_{\alpha'}L_{\alpha'}, N_{\beta'}L_{\beta'}\rangle. \end{aligned} \tag{B2}$$

The 2D isotropic harmonic oscillators with principle quantum number $N \le 9$ are included in the full-symmetric Hartree–Fock mean field calculation. $\langle\psi^\dagger_{\alpha\zeta}\psi_{\alpha'\zeta}\rangle$ and $\langle\psi^\dagger_{\alpha\zeta}\psi_{\beta'\zeta'}\rangle$ are order parameters with respect to the ground state for every iteration step. They satisfy the symmetry constraints as follows. $\langle\psi^\dagger_{\alpha\uparrow}\psi_{\beta\uparrow}\rangle = \langle\psi^\dagger_{\alpha\downarrow}\psi_{\beta\downarrow}\rangle$ and $\langle\psi^\dagger_{\alpha\uparrow}\psi_{\beta\downarrow}\rangle = \langle\psi^\dagger_{\alpha\downarrow}\psi_{\beta\uparrow}\rangle = 0$ because of $SU(2)_\zeta$ symmetry. M_y symmetry gives $\langle\psi^\dagger_{\alpha\zeta}\psi_{\beta\zeta'}\rangle = \langle\psi^\dagger_{\bar{\alpha}\zeta}\psi_{\bar{\beta}\zeta'}\rangle$. And spinless TR symmetry gives

$\langle\psi^{\dagger}_{\alpha\zeta}\psi_{\beta\zeta'}\rangle = \langle\psi^{\dagger}_{\bar{\beta}\zeta'}\psi_{\bar{\alpha}\zeta}\rangle$. Because of continues rotation symmetry, $\langle\psi^{\dagger}_{\alpha\zeta}\psi_{\beta\zeta'}\rangle = \delta_{L_\alpha,L_\beta}\langle\psi^{\dagger}_{\alpha\zeta}\psi_{\beta\zeta'}\rangle$. Here $\bar{\alpha}$ is the time reversal state of α.

Because for one N, smaller $|L|$ means a state with lower angular momentum, corresponding to more localized wavefunctions of lower potential energy but larger interaction energy. The energies of oscillator states with different $|L|$ will be different for a fixed N (two-fold degeneracy $E_{(N,L)} = E_{(N,-L)}$ remains because of M_y and T symmetries). Thus, under the meaning of mean field, 'single particle' levels s, p still have the same degeneracy as the zero-interaction limit, which is 1-fold and 2-fold, respectively. But d levels split into '$2+1$' fold.

Appendix C: Effective lattice model with strong SOC

The effective lattice model in two splitted degenerate subspaces on square lattice is given below. When the SOC effect is strong, the symmetry group is double point group D_4^D, The representation matrices of D_4^D group's generators and time reversal operation under two degenerate many-body basis labeled $|J,M_j\rangle$ are

$$D(C_{4z}) = \mathrm{e}^{-\mathrm{i}\frac{\pi}{2}M_jZ},\ \ D(M_y) = -\mathrm{i}X,\ \ D(T) = \mathrm{i}Y, \quad \text{(C1)}$$

where X,Y,Z are pauli matrices acting on the total angular momentum degree of freedom of electron fields. The Hamiltonian satisfing these symmetry constraints should be as follows (the energy shift term $1_{\boldsymbol{R}}1_{\boldsymbol{R}'}$ is omitted):

$$\begin{aligned} H =& \sum_{\langle\boldsymbol{R},\boldsymbol{R}'\rangle_{\boldsymbol{x}}}\left[h_{xx}X^{\boldsymbol{R}}X^{\boldsymbol{R}'} + h_{yy}Y^{\boldsymbol{R}}Y^{\boldsymbol{R}'}\right] \\ &+ \sum_{\langle\boldsymbol{R},\boldsymbol{R}'\rangle_{\boldsymbol{y}}}\left[h_{yy}X^{\boldsymbol{R}}X^{\boldsymbol{R}'} + h_{xx}Y^{\boldsymbol{R}}Y^{\boldsymbol{R}'}\right] \\ &+ \sum_{j=1}^{2}\sum_{\langle\boldsymbol{R},\boldsymbol{R}'\rangle_j} D(C_{4z})^{j-1}\times\left[aYZ + bZY\right]^{\langle\boldsymbol{R},\boldsymbol{R}'\rangle_j} \\ &\times D(C_{4z})^{1-j}, \end{aligned} \quad \text{(C2)}$$

where $\langle\boldsymbol{R},\boldsymbol{R}'\rangle_{\boldsymbol{x}/\boldsymbol{y}}$ denotes nearest bonds along x/y-direction and $\boldsymbol{R}$ goes through all sites. $\langle\boldsymbol{R},\boldsymbol{R}'\rangle_j$ $(j=1,2)$ denotes nearest bonds related to each other by C_{4z} symmetry, and $\langle\boldsymbol{R},\boldsymbol{R}'\rangle_1$ along x-axis. $D(C_{4z}) = \mathrm{e}^{-\mathrm{i}\frac{\pi}{4}Z}$ gives the Hamiltonian in degenerate $|J=\frac{1}{2},M_j=\pm\frac{1}{2}\rangle$ space. $D(C_{4z}) = \mathrm{e}^{-\mathrm{i}\frac{3\pi}{4}Z}$ gives the Hamiltonian in degenerate $|J=\frac{3}{2},M_j=\pm\frac{3}{2}\rangle$ space in Eq. (C2). Because of times reversal symmetry, ZZ term is still forbidden.

Appendix D: The Hamiltonian of exchange and superexchange interactions

For exchange interaction and superexchange interaction, it is noticed that there is no $SU(2)_\zeta$ symmetry for a single site now. Thus, the spin index cannot be ignored anymore. There are four bases in G.S. manifold, as shown in Eq. (16) in the weak interaction condition.

The representation matrices $D(g)$ under four many-body bases Eq. (16) are

$$\begin{aligned} &D(C_{4z}) = -ZZS_0S_0,\ \ D(M_y) = XXS_0S_0, \\ &D(\mathcal{T}) = -XXS_yS_y, \end{aligned} \quad \text{(D1)}$$

where X, Y, Z are Pauli matrices acting on the orbital degree of freedom, and S_x, S_y, S_z are Pauli matrices acting on the spin degree of freedom. There is still $SU(2)_\zeta$ symmetry for one bond, the Hamiltonian of one bond should commute with S_x, S_y, and S_z. According to the symmetries above, the form of the Hamiltonian for spin can be only S_0S_0 or $S_xS_x+S_yS_y+S_zS_z$. The real space Hamiltonian can be $X_{\boldsymbol{R}}X_{\boldsymbol{R}'}$, $Y_{\boldsymbol{R}}Y_{\boldsymbol{R}'}$, $Z_{\boldsymbol{R}}Z_{\boldsymbol{R}'}$, $X_{\boldsymbol{R}}1_{\boldsymbol{R}'}$, $1_{\boldsymbol{R}}X_{\boldsymbol{R}'}$ and $1_{\boldsymbol{R}}1_{\boldsymbol{R}'}$ terms. The lattice Hamiltonian has the general form as follows:

$$\begin{aligned} H =& \sum_{\langle\boldsymbol{R},\boldsymbol{R}'\rangle}\Big[\left(aX_{\boldsymbol{R}}X_{\boldsymbol{R}'} + bY_{\boldsymbol{R}}Y_{\boldsymbol{R}'} + cZ_{\boldsymbol{R}}Z_{\boldsymbol{R}'}\right)\boldsymbol{S}_{\boldsymbol{R}}\boldsymbol{S}_{\boldsymbol{R}'} \\ &+ \left(a'X_{\boldsymbol{R}}X_{\boldsymbol{R}'} + b'Y_{\boldsymbol{R}}Y_{\boldsymbol{R}'} + c'Z_{\boldsymbol{R}}Z_{\boldsymbol{R}'}\right)S_{0\boldsymbol{R}}S_{0\boldsymbol{R}'} \\ &+ h\boldsymbol{S}_{\boldsymbol{R}}\boldsymbol{S}_{\boldsymbol{R}'}\Big] \\ &+ \sum_{j=1}^{2}\sum_{\langle\boldsymbol{R},\boldsymbol{R}'\rangle_j} D(C_{4z})^{j-1}\Big[e(X_{\boldsymbol{R}}1_{\boldsymbol{R}'} + 1_{\boldsymbol{R}}X_{\boldsymbol{R}'})\boldsymbol{S}\cdot\boldsymbol{S} \\ &+ f(1_{\boldsymbol{R}}X_{\boldsymbol{R}'} + X_{\boldsymbol{R}}1_{\boldsymbol{R}'})S_0S_0\Big]^{\langle\boldsymbol{R},\boldsymbol{R}'\rangle_j} D(C_{4z})^{1-j}, \end{aligned} \quad \text{(D2)}$$

where a,b,c,a',b',c',h,e,f are real coefficients. $\langle\boldsymbol{R},\boldsymbol{R}'\rangle$ denotes nearest bonds. $\langle\boldsymbol{R},\boldsymbol{R}'\rangle_j$ $(j=1,2)$ denotes two bonds related to each other by C_{4z} symmetry, and $\langle\boldsymbol{R},\boldsymbol{R}'\rangle_1$ along x-direction.

Acknowledgments

Project supported by the National Natural Science Foundation of China (Grant No. 12274005), the National Key Research and Development Program of China (Grant No. 2021YFA1401903), and Innovation Program for Quantum Science and Technology (Grant No. 2021ZD0302403).

References

[1] Cao Y, Fatemi V, Demir A, Fang S A, Tomarken S L, Luo J Y, Sanchez-Yamagishi J D, Watanabe K, Taniguchi T, Kaxiras E, Ashoori R C and Jarillo-Herrero P 2018 *Nature* **556** 80

[2] Cao Y, Fatemi V, Fang S, Watanabe K, Taniguchi T, Kaxiras E and Jarillo-Herrero P 2018 *Nature* **556** 43
[3] Mak K F and Shan J 2022 *Nat. Nanotechnol.* **17** 686
[4] Devakul T, Crépel V, Zhang Y and Fu L 2021 *Nat. Commun.* **12** 6730
[5] Bi Z, Yuan N F Q and Fu L 2019 *Phys. Rev. B* **100** 035448
[6] Xu Y, Liu S, Rhodes D A, Watanabe K, Taniguchi T, Hone J, Elser V, Mak K F and Shan J 2020 *Nature* **587** 214
[7] Kennes DM, Claassen M, Xian LD, Georges A, Millis A J, Hone J, Dean C R, Basov D N, Pasupathy A N and Rubio A 2021 *Nat. Phys.* **17** 155
[8] Spanton E M, Zibrov A A, Zhou H X, Taniguchi T, Watanabe K, Zaletel M P and Young A F 2018 *Science* **360** 62
[9] Jin C H, Regan E C, Yan A M, Iqbal Bakti Utama M, Wang D Q, Zhao S H, Qin Y, Yang S J, Zheng Z R and Shi S Y 2019 *Nature* **567** 76
[10] Zhang X, Tsai K T, Zhu Z Y, Ren W, Luo Y J, Carr S, Luskin M, Kaxiras E and Wang K 2021 *Phys. Rev. Lett.* **127** 166802
[11] Wu F F, Li L, Xu Q L, Liu L, Yuan Y L, Zhao J J, Huang Z H, Zan X Z, Watanabe K, Taniguchi T, Shi D X, Xian L D, Yang W, Du L J and Zhang G Y 2023 *Chin. Phys. Lett.* **40** 047303
[12] Wu F C, Lovorn T, Tutuc E and MacDonald A H 2018 *Phys. Rev. Lett.* **121** 026402
[13] Tang Y H, Li L Z, Li T X, Xu Y, Liu S, Barmak K, Watanabe K, Taniguchi T, MacDonald A H and Shan J 2020 *Nature* **579** 353
[14] Wu F C, Lovorn T, Tutuc E, Martin I and MacDonald A H 2019 *Phys. Rev. Lett.* **122** 086402
[15] Cai J, Anderson E, Wang C, Zhang X, Liu X, Holtzmann W, Zhang Y, Fan F, Taniguchi T, Watanabe K, *et al*. 2023 *Nature* **622** 63
[16] Zeng Y H, Xia Z C, Kang K F, Zhu J C, Knüppel P, Vaswani C, Watanabe K, Taniguchi T, Mak K F and Shan J 2023 *Nature* **622** 69
[17] Park H J, Cai J Q, Anderson E, Zhang Y N, Zhu J Y, Liu, X Y, Wang C, Holtzman W, Hu C W, Liu Z Y, Taniguchi T, Watanabe K, Chu J H, Cao T, Fu L, Yao W, Chang C Z, Cobden D, Xiao D and Xu X D 2023 *Nature* **622** 74
[18] Xu F, Sun Z, Jia T T, Liu C, Xu C, Li C S, Gu Y, Watanabe K, Taniguchi T, Tong B B, Jia J F, Shi Z W, Jiang S W, Zhang Y, Liu X X and Li T X 2023 *Phys. Rev. X* **13** 031037
[19] Li T X, Jiang S W, Shen B W, Zhang Y, Li L Z, Tao Z, Devakul T, Watanabe K, Taniguchi T and Fu L 2021 *Nature* **600** 641
[20] Li H Y, Xiang Z Y, Reddy A P, Devakul T, Sailus R, Banerjee R, Taniguchi T, Watanabe K, Tongay S and Zettl A 2024 *Science* **385** 86
[21] Reddy A P, Devakul T and Fu L 2023 *Phys. Rev. Lett.* **131** 246501
[22] Luo D, Reddy A P, Devakul T and Fu L 2023 arXiv:2303.08162 [cond-mat.str-el]
[23] Yannouleas C and Landman U 2023 *Phys. Rev. B* **108** L121411
[24] Qi Y and Wei J H 2024 *Chin. Phys. B* **33** 057301
[25] Zhang Y, Yuan N F Q and Fu L 2020 *Phys. Rev. B* **102** 201115
[26] Wu F C, Lovorn T and MacDonald A H 2018 *Phys. Rev. B* **97** 035306
[27] Chan Y H, Jiang H C and Chen Y C 2023 *Phys. Rev. B* **107** 214402